RESEARCH PAPER

Ex vivo coronary calcium volume quantification using a high-spatial-resolution clinical photon-counting-detector computed tomography

Jeffrey F. Marsh Jr., Patrick D. VanMeter, Kishore Rajendran, Shuai Leng, and Cynthia H. McCollough*

Mayo Clinic, Department of Radiology, Rochester, Minnesota, United States

ABSTRACT. **Purpose:** Coronary artery calcification (CAC) is an important indicator of coronary disease. Accurate volume quantification of CAC is challenging using computed tomography (CT) due to calcium blooming, which is a consequence of limited spatial resolution. *Ex vivo* coronary specimens were scanned on an ultra-high-resolution (UHR) clinical photon-counting detector (PCD) CT scanner, and the accuracy of CAC volume estimation was compared with a state-of-the-art conventional energy-integrating detector (EID) CT, a previous-generation investigational PCD-CT, and micro-CT.

Approach: CAC specimens ($n = 13$) were scanned on EID-CT and PCD-CT using matched parameters (120 kV, 9.3 mGy CTDI$_{vol}$). EID-CT images were reconstructed using our institutional routine clinical protocol for CAC quantification. UHR PCD-CT data were reconstructed using a sharper kernel. An image-based denoising algorithm was applied to the PCD-CT images to achieve similar noise levels as EID-CT. Micro-CT images served as the volume reference standard. Calcification images were segmented, and their volume estimates were compared. The CT data were further compared with previous work using an investigational PCD-CT.

Results: Compared with micro-CT, CT volume estimates had a mean absolute percent error of $24.1\% \pm 25.6\%$ for clinical PCD-CT, $60.1\% \pm 48.2\%$ for EID-CT, and $51.1\% \pm 41.7\%$ for previous-generation PCD-CT. Clinical PCD-CT absolute percent error was significantly ($p < 0.01$) lower than both EID-CT and previous generation PCD-CT. The mean calcification CT number and contrast-to-noise ratio were both significantly ($p < 0.01$) higher in clinical PCD-CT relative to EID-CT.

Conclusions: UHR clinical PCD-CT showed reduced calcium blooming artifacts and further enabled improved accuracy of CAC quantification beyond that of conventional EID-CT and previous generation PCD-CT systems.

© 2023 Society of Photo-Optical Instrumentation Engineers (SPIE) [DOI: 10.1117/1.JMI.10.4.043501]

Keywords: photon counting detector computed tomography; coronary artery disease; coronary calcifications; calcium quantification; image domain denoising

Paper 22253GR received Sep. 21, 2022; revised Apr. 17, 2023; accepted Jun. 20, 2023; published Jul. 4, 2023.

1 Introduction

The development of coronary artery calcification (CAC) is an indication of coronary artery disease and atherosclerosis.[1–4] The presence of CAC is associated with increased risk of major cardiac events, and the proactive screening for calcium deposits in asymptomatic patients improves

---

*Address all correspondence to Cynthia McCollough, mccollough.cynthia@mayo.edu

cardiovascular risk assessment.[5] The size of coronary calcifications and degree of luminal stenosis are commonly assessed using coronary computed tomography (CT) angiography exams.[6–9] Calcified deposits within vessel walls present as brighter pixels in CT images due to their high attenuation. This characteristic enables volume quantification of the calcifications through image segmentation.

The accuracy of CAC volume estimation in conventional energy-integrating detector CT (EID-CT) is limited due to the blooming artifacts caused by insufficient spatial resolution.[10,11] The size of the detector pixel and the use of separating septa between individual detectors are significant contributors to the resolution limitations in EID-CT systems. On the other hand, photon-counting detector CT (PCD-CT) technology utilizes smaller detector pixels and does not require interpixel septa.[12–15] As a result, PCD-CT has demonstrated higher spatial resolution at routine doses,[12,16–19] which can reduce the blooming effect and consequently improve volume estimation accuracy.[20] Recent investigations focusing on the application of PCD-CT technology for the assessment of CAC have shown much promise over conventional EID-CT in terms of detectability,[21] calcium scoring accuracy,[22,23] image quality,[24] and volume quantification.[25–27]

A clinical ultra-high-resolution (UHR) PCD-CT system has recently been approved for use in clinical practice and is now available for patient CT applications.[23,24,28] This clinical PCD-CT system has a higher resolution detector collimation (120×0.2 mm), which uses a very small detector pixel size (151 μm $\times$ 176 μm at isocenter). The detector pixel size of this new PCD technology is smaller than that used in a previous study,[27] which investigated CAC volume estimation accuracy in *ex vivo* specimens on an earlier prototype PCD-CT system. Such reductions in detector pixel size may enable reductions in calcification blooming and improvements in volume quantification accuracy. Therefore, the aim of this study is to specifically assess further improvements to CAC volume quantification made possible using the UHR acquisition mode of the clinical PCD-CT scanner and to compare with a state-of-the-art third-generation clinical dual-source EID-CT scanner and a previous-generation prototype PCD-CT system. Associated improvements would be fundamentally enabled by reductions in partial volume averaging at the axial edges of the CAC specimens, and thus our study focuses on a static scanning scenario to eliminate contributing inaccuracies incurred by cardiac motion artifacts. The same *ex vivo* human cadaveric specimens were used in this application as previous work[20,27] to facilitate such volumetric comparisons.

2 Methods

2.1 Specimen Preparation and Calcification Identification

This work was approved by our Mayo Clinic Institutional Biospecimens Committee (Rochester, Minnesota, United States). Six coronary artery specimens and one coronary venous graft were excised from three human cadavers. All excised specimens were fixed in neutral-buffered formalin and embedded in methyl methacrylate (MMA) blocks. Thirteen clinically relevant calcification deposits were identified among those seven coronary specimens in previous work by Sandstedt et al.[27] The 13 resultant specimens included 12 CACs and a single calcification from the coronary venous graft. In this study, we assess the same 13 calcifications to enable comparisons with the results from the previous work.

2.2 Data Acquisition and Image Reconstruction

The coronary artery specimens were placed into a 30-cm body-shaped water tank and scanned on a third-generation dual-source EID-CT scanner (SOMATOM Force, Siemens Healthineers, Forchheim, Germany) and a clinical full-body dual-source PCD-CT scanner (NAEOTOM Alpha, Siemens Healthineers, Forchheim, Germany).[28] The scan and reconstruction parameters are summarized in Table 1.

Images were reconstructed using each platform's native iterative reconstruction technique. EID-CT images were reconstructed using a routine quantitative kernel (Qr49; 0% MTF at 12.4 lp/cm), following the standard protocol in our practice, whereas the higher resolution PCD-CT data were reconstructed with a sharper quantitative kernel (Qr68; 0% MTF at 15.5 lp/cm).

Table 1 Acquisition and reconstruction parameters for the EID-CT and PCD-CT imaging systems.

Parameter	EID-CT	PCD-CT
Scanner model	SOMATOM force	NAEOTOM alpha
Scan mode	Spiral	Spiral
CTDIvol (mGy)	9.32	9.36
Tube voltage (kV)	120	120
Tube current–time product (mAs)	136	117
Pitch	0.5	0.5
Collimation (mm)	128 × 0.6	120 × 0.2
Rotation time (s)	0.5	0.33
Reconstruction algorithm	ADMIRE (3)	QIR (3)
Reconstruction kernel	Qr49	Qr68
Denoising algorithm	None	Slice-PKAID[29]
Slice thickness (mm)	0.6	0.6
Increment (mm)	0.6	0.6
Reconstruction field of view (mm)	120	120
Image matrix size	512 × 512	512 × 512

Images obtained from a micro-CT scanner were used to establish a reference volume due to the non-destructive and high-resolution imaging capability offered by such systems.[30–33] In this study, an in-house micro-CT scanner (Mayo Clinic X-ray Imaging Core)[34] was used to individually image each coronary specimen. The detector was a Pixis-XB detector (Pixis-XB: 1300, Princeton Instruments, Trenton, New Jersey, United States) featuring a 20 μm pixel pitch. The x-ray source (XRD C-Tech Tube, PANalytical, Eindhoven, Netherlands) featured a molybdenum anode. The micro-CT images were reconstructed using an in-house Feldkamp algorithm. The corresponding micro-CT volume estimations were treated as the reference and were used to assess the accuracy of the measurements obtained from PCD-CT and EID-CT systems.

2.3 PCD-CT Image Domain Denoising

Image noise was estimated by measuring the standard deviation within circular regions of interest (ROIs) positioned in the water surrounding the calcification specimens. The sharper quantitative kernel used to produce the PCD images was better suited to resolving the higher frequencies captured by the higher resolution PCD detector; however, it also increased high-frequency noise. Thus an image domain denoising algorithm was used to limit the influence of high-frequency noise on the ensuing PCD-CT calcification volume measurements. A prior knowledge-based noise-reduction algorithm, Slice-PKAID,[29] was therefore applied to the PCD-CT data to achieve a noise level similar to that observed in the EID-CT images.

2.4 Segmentation and Analysis

Segmentation was performed using a half-maximum thresholding (HMT) methodology previously described in the literature.[20,27,35–37] This methodology is designed to minimize the impact of blooming on volume estimation for highly attenuating objects with a relatively uniform composition. Briefly, the user needed to manually position a small ROI into the central most attenuating region of the calcification [e.g., black arrow in Fig. 1(a)]. To do this effectively, the user had to adjust the grayscale window level/width image-by-image to reveal the most attenuating region of the calcification. Frequently, the first and last images of the calcification were very low in
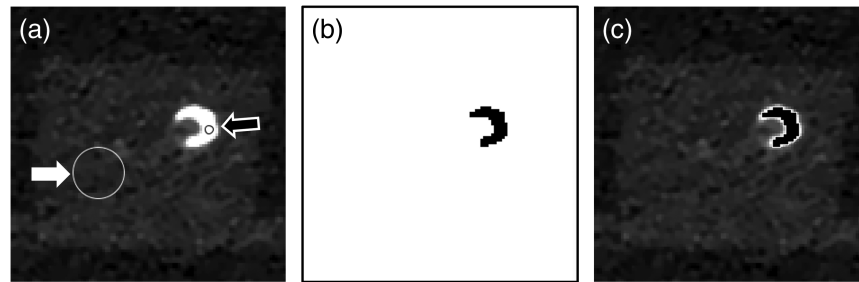
Fig. 1 Schematic illustrating the segmentation process. (a) The original PCD-CT image of a sample calcification specimen (23.4 × 23.4 mm² field of view). The circular ROIs selections for calcification (black arrow) and background (white arrow) used for determining the HMT are shown. Window level/width: 398/995 HU. (b) Segmentation mask displaying voxels above the HMT (black shaded). (c) Overlay of the segmentation mask onto the original CT image. The bright halo around the mask is representative of the blooming artifact.

attenuation due to significant partial volume averaging at the ends; in such cases, the HMT from an adjacent (more centrally located) image was used. Another circular ROI was placed in the background MMA [e.g., the white arrow in Fig. 1(a)]. The average and standard deviations of the CT numbers were calculated within each ROI, and the threshold for HMT segmentation was set as the halfway point between the two averages. Further, the ROI measurements from the PCD-CT and EID-CT scanners were compared and used to calculate the contrast-to-noise ratio (CNR). The HMT segmentation procedure is illustrated in Fig. 1.

2.5 Calcification Volume Assessment

Calcification segmentation was performed image-by-image, and the resulting segmented area included all voxels within the calcification that exceeded the HMT threshold. The segmented calcification areas obtained from contiguous CT images were then added to yield the calcification volume in voxels. The calcification volume was further converted to mm³ by multiplying the voxel count with the volume of an individual voxel (determined by the reconstruction field of view and image matrix size). This process was performed identically for all calcification specimens and for all imaging systems: EID-CT, PCD-CT, and micro-CT. The final calcification volumes obtained from the EID-CT and PCD-CT data were normalized to the micro-CT reference volume.

2.6 Comparison with Previous-Generation PCD-CT

The calcification volume measurements reported herein were further compared with results reported in earlier work by our group, which examined the same *ex vivo* specimens using a previous-generation investigational PCD-CT scanner.[27] That PCD-CT system (SOMATOM CounT, Siemens Healthineers) was built upon a modified second-generation dual-source SOMATOM Flash system. The previous acquisitions were performed using a UHR mode, which featured an isocenter detector pixel size of $250 \times 250\ \mu m^2$ and had a limited 275 mm field of view. This is in contrast to the $151 \times 176\ \mu m^2$ detector pixel size featured by the NAEOTOM Alpha.

2.7 Statistical Analysis

The mean absolute percent error in calcification volume estimates is reported for each CT system model. The Wilcoxon Sign Rank Test is used to assess the statistical significance of the differences in absolute percent error between the clinical PCD-CT and EID-CT, as well as between the clinical PCD-CT and the previous generation PCD-CT. The mean calcification CT number and mean CNR are reported for both the clinical PCD-CT and EID-CT, and the Wilcoxon Sign Rank Test is used to assess the statistical significance. Statistical analyses were performed using MATLAB (vers. 2021b, The MathWorks Inc., Natick, Massachusetts, United States).
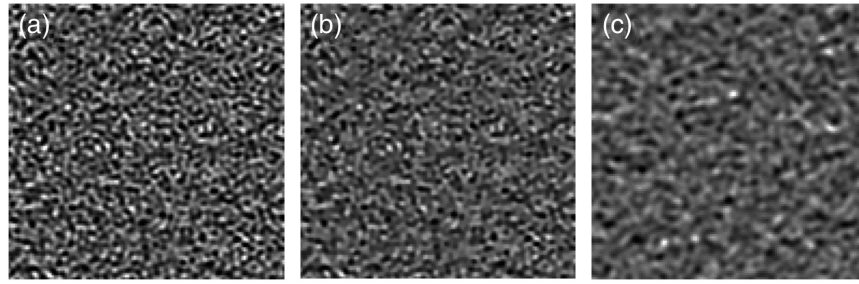
Fig. 2 Comparison of noise magnitude and texture in a 128×128 pixel section of the water surroundings (window level/width: 40/400 HU) between (a) PCD-CT (original), (b) PCD-CT (denoised), and (c) EID-CT. Noise magnitude is similar in (b) and (c), but noise texture is not identical.

3 Results

3.1 Impact of PCD-CT Denoising

The image noise within the Qr49 EID-CT images was measured as 42.6 ± 0.9 HU, and the image noise within the original Qr68 PCD-CT images was measured as 74.0 ± 1.3 HU. After application of the Slice-PKAID denoising algorithm, the PCD-CT image noise was reduced to 34.8 ± 0.9 HU, which was comparable to that of the EID-CT (Fig. 2).

3.2 Attenuation and Contrast Measurements

Measurements were obtained from the central image of each calcification specimen and are summarized in Fig. 3. The average calcification contrast and CNR were calculated among the 13 specimens, and both quantities were found to be higher in the PCD-CT data. On average, the calcification mean CT number was found to be 373.2 ± 113.4 HU higher in PCD-CT, the mean of the background MMA was 11.5 ± 6.9 HU higher in EID-CT, and the standard deviation of the background MMA was 7.6 ± 7.6 HU higher in EID-CT. The mean CNR calculated across all images of all specimens was found to be 26.56 ± 2.30 for the PCD-CT and 12.43 ± 1.14 for EID-CT.

3.3 Calcification Volume Assessment

Figure 4 presents an example comparison of a calcification specimen between micro-CT, PCD-CT, and EID-CT images. The higher spatial resolution of the micro-CT mitigates blooming artifacts that are otherwise evident in the EID-CT and PCD-CT images. However, the degree of blooming artifacts is substantially reduced on the PCD-CT image compared with the EID-CT image, resulting in a better delineation of the lumen. Figure 5 shows another specimen and the corresponding segmentation. Figures 5(b) and 5(c) display the calcification specimen in PCD-CT and EID-CT images, respectively, and further includes the superimposed boundary of the segmented area. A reduced segmented area (5.4 versus 7.3 mm^2) can be noted in the PCD-CT image, indicating reduced blooming. The specific calcification volume measurements are summarized in Table 2. For all 13 specimens, the PCD-CT images resulted in a smaller
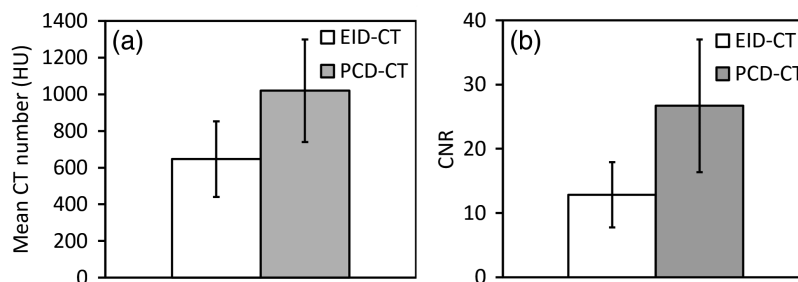

Fig. 3 (a) The mean CT number measured from all 13 specimens for both EID-CT and PCD-CT data. Error bars denote the standard deviation. (b) The CNR was calculated for all specimens.
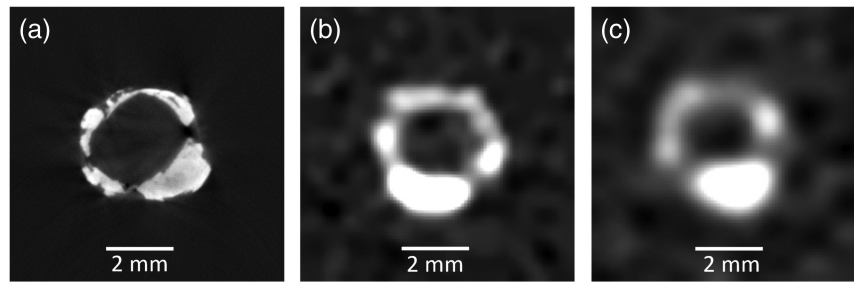
Fig. 4 Example calcification specimen images from (a) micro-CT, (b) PCD-CT, and (c) EID-CT images with an 8×8 mm field of view [CT images in (b) and (c) have window level/width: 380/815 HU]. Compared with EID-CT, PCD-CT shows significantly decreased blooming.
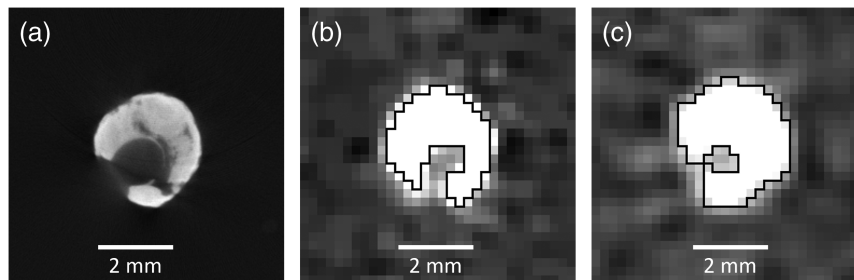

Fig. 5 Example calcification specimen from (a) micro-CT, (b) PCD-CT, and (c) EID-CT imaged with a 7.5×7.5 mm^2 field of view [CT images in (b) and (c) have window level/width: 240/615 HU]. The boundaries of the segmented calcification areas were superimposed onto the CT images. The PCD-CT image shows significantly decreased blooming. The PCD-CT image also correctly reveals that the calcium does not form a closed loop, which cannot be determined in the EID-CT image.

Table 2 Results of the calcification specimen volume measurements as made within the micro-CT, EID-CT, and PCD-CT images. The higher resolution micro-CT serves as the volume reference for the study.

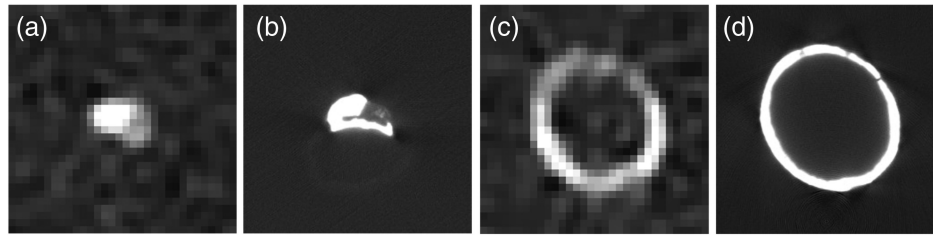| Specimen	Micro-CT (mm^3)	EID-CT (mm^3)	PCD-CT (mm^3)
1	8.5	9.4	8.5
2	6.2	7.8	5.5
3	2.7	6.4	3.3
4	3.9	7.9	5.6
5	14.6	19.8	13.8
6	44.0	55.4	52.1
7	32.3	46.1	39.8
8	66.5	170.2	131.6
9	9.9	19.2	13.5
10	45.0	64.9	49.2
11	2.8	4.7	3.6
12	15.5	20.6	17.3
13	40.7	43.1	38.2

Fig. 6 Calcification morphologies observed with small size and thin shape. First is the small oval-shaped calcification morphology as shown in (a) clinical PCD-CT and (b) micro-CT. The small axial area incurs more severe blurring with surrounding media. Second is the thin ring-like shaped calcification morphology as shown in (c) clinical PCD-CT and (d) micro-CT. The thin ring is susceptible to blurring both inwardly and outwardly. The CT images in (a) and (c) have window level/width 975/380 HU and 7.5×7.5 mm^2 field of view.

volume estimation compared with EID-CT. In 12/13 cases, the PCD-CT volume estimate is closer to the micro-CT reference volume, whereas in the remaining case, PCD-CT underestimates micro-CT by approximately the same amount as EID-CT overestimates it. The mean absolute percent error relative to the micro-CT reference standard was calculated for the CT CAC volume estimates and was found to be 24.1% $\pm$ 25.6% for clinical PCD-CT and 60.1% $\pm$ 48.2% for EID-CT. Additionally, it was observed that specific calcification morphologies could exacerbate CT volume segmentation inaccuracies, such as having a small size or thin shape; Fig. 6 showcases two such examples.

3.4 Comparison with Previous-Generation PCD-CT

A graphical comparison of the CAC volume measurement accuracy for three CT scanner systems (i.e., SOMATOM Force EID-CT, investigational SOMATOM CounT PCD-CT, and clinical NAEOTOM Alpha PCD-CT) is shown in Fig. 7. The error in the calcification volume estimates obtained from CT data is expressed as a percent of the micro-CT reference volume. The previous-generation investigational PCD-CT scanner yielded more accurate volume estimates than the EID-CT for 8/13 specimens evaluated. The current-generation clinical PCD-CT scanner obtained smaller and more accurate volume measurements for 12/13 specimens compared with the previous-generation PCD-CT, and the remaining specimen differed by only 0.7 mm^3. Further, the CAC volume estimates from the previous-generation PCD-CT were found to have a mean absolute percent error of 51.1% $\pm$ 41.7% relative to the micro-CT reference standard, compared with the 24.1% $\pm$ 25.6% calculated for the clinical PCD-CT. Figure 8 displays the differences in volume distribution across the individual specimens as measured with the three CT scanners.
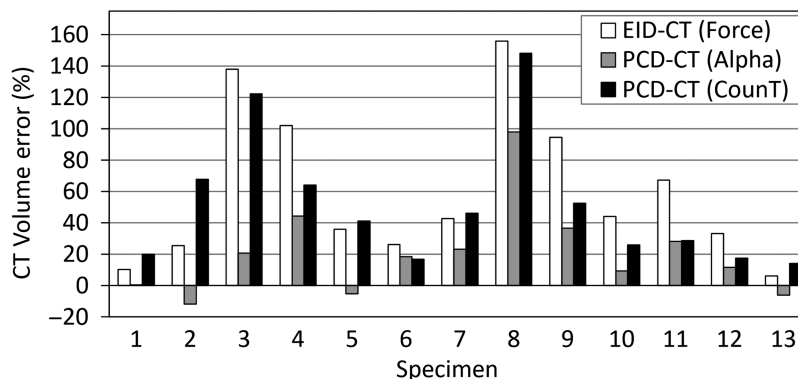

Fig. 7 Error in the calcification volume estimates obtained from CT data is expressed as a percent of the micro-CT reference volume (i.e., 0% error equals micro-CT volume). Errors in CT volume estimates are presented for the state-of-the-art EID-CT (force), the current-generation clinical PCD-CT (alpha), and the previous-generation investigational PCD-CT (CounT).
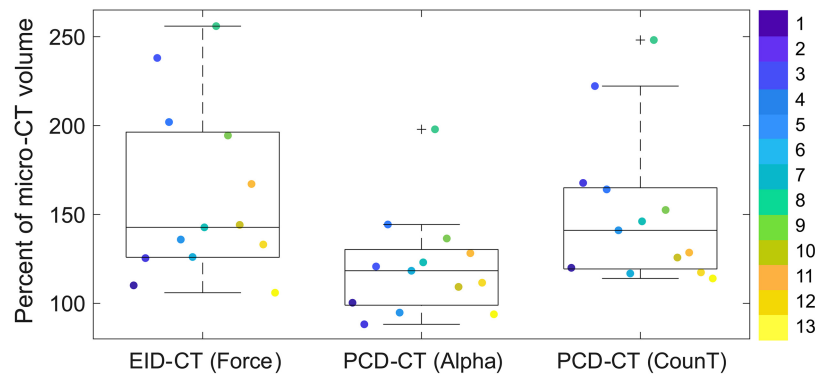
Fig. 8 Individual calcification volumes are displayed in box scatter plots as a percentage of the micro-CT volume (i.e., 100% mark designates a CT volume estimation identical to the micro-CT reference volume). The 13 calcifications are color coded to enable specimen-to-specimen volume accuracy comparisons between CT scanners. The EID-CT (force) data are displayed on the left, the clinical PCD-CT (alpha) data are displayed in the middle, and the investigational PCD-CT (CounT) data are displayed on the right. In each box plot, the central horizontal line indicates the median of the specimen volumes. The upper and lower box edges indicate the 75th and 25th percentiles, respectively. The upper and lower whiskers extend to the nonoutlier maximum and nonoutlier minimum, respectively. Outliers are denoted by "+." The calcification volumes for the clinical PCD-CT (alpha) had a lower median and a tighter distribution relative to the previous generation PCD-CT (CounT) and EID-CT (force).

3.5 Statistical Analysis

The mean absolute percent error for the estimated calcification volume was calculated from all 13 specimens and was discovered to be lowest in the clinical PCD-CT data. The observed differences in absolute percent error between the clinical PCD-CT and both the clinical EID-CT and previous generation PCD-CT were found to be statistically significant ($p < 0.01$) using the Wilcoxon Sign Rank Test. The mean calcification CT number and mean CNR were found to be greater for the clinical PCD-CT data than EID-CT data, and the Wilcoxon Sign Rank Test revealed a statistically significant difference ($p < 0.01$) in both evaluations.

4 Discussion

Evaluation of CAC volume using a clinical PCD-CT system demonstrated increased accuracy compared with EID-CT, relative to the micro-CT reference. The PCD technology enables smaller detector pixels, which allows CT scans to attain higher spatial resolution than conventional EID-CT technology. Although the size of EID-CT detector elements can also be decreased, this would reduce the detector geometric efficiency (fill factor), considering that the thickness of septa cannot be substantially reduced.[16,18,38–40] PCDs do not require interpixel septae and can therefore accommodate smaller detector pixels without losing geometric efficiency. Sharper convolution kernels are needed for PCD-CT reconstructions to take advantage of the higher resolution scan data. Although the sharp kernels can resolve higher frequency information, they also increase high-frequency noise. Such image noise can be reasonably reduced by deploying denoising algorithms. Here we used the Slice-PKAID image domain denoising algorithm to reduce the noise in the PCD-CT images to similar levels as in the EID-CT images with a smoother kernel.

The segmented volume of several calcification specimens reported in Table 2 shows greater discrepancies between clinical PCD-CT and micro-CT, namely, specimens 4, 8, 9, and 11. Upon further inspection, these discrepancies appear to be caused by unique calcification morphologies, as relate to their size and shape. Specimens 4 and 11 were observed to be small oval-shaped calcifications [e.g., Figs. 6(a) and 6(b)] and were found to have a small axial area relative to the other specimens. Meanwhile, specimens 8 and 9 were found to be thin ring-like shaped calcifications [e.g., Figs. 6(c) and 6(d)] spanning the vessel wall circumference. Both morphologies, thin ring-like shaped and small oval-shaped, were found to have the lowest HMT values relative to all other calcifications evaluated. These findings suggest that such calcification morphologies are more extensively impacted by partial volume averaging related blurring in the CT images.

Such conditions could reduce the true maximum calcification attenuation and cause a decreased HMT value, which in turn could lead to a larger segmented axial area per image, inevitably leading to a larger total volume and contributing to the observed volume deviations for these specimens.

The CNR values calculated from all calcification specimens were found to be more than double the magnitude for PCD-CT data (26.56 ± 2.30) relative to EID-CT data (12.43 ± 1.14). The major contributor to the higher CNR was determined to be the contrast of the calcifications, which was ~375 HU higher on average in the PCD-CT images relative to the EID-CT images. There are two primary factors contributing to the observed increase in calcification contrast in the PCD-CT data. First is the decreased partial volume averaging occurring around the boundaries of the calcification. This is directly related to the increased spatial resolution of the PCD technology. Second is the photon weighting in the PCD technology, which provides a higher contrast compared with the energy weighting in EID.[12,28,41]

The CT number measurements yielded from the calcification specimens were observed to be significantly larger in the PCD-CT data relative to the EID-CT. Importantly, these larger values observed in PCD-CT would have a significant impact on the standard calcium scoring methodology. The Agatston score was initially described by Agatston et al.[42] and requires data acquisition using the 120 kVp tube potential for conventional EID-CT scanners. However, recent work has demonstrated that using virtual monoenergetic images at 70 keV for the PCD-CT data results in comparable energy spectrum to the standard 120 kV spectrum used for EID-CT.[23,43–46]

Previous work presented by Sandstedt et al.[27] similarly demonstrated improved CAC volume quantification accuracy using an investigational SOMATOM CounT PCD-CT. However, that technology featured detector pixel sizes of $250 \times 250~\mu m^2$ (at isocenter), whereas the current NAEOTOM Alpha is capable of pixel sizes as small as $150 \times 176~\mu m^2$ in UHR mode, yielding a reduction in the detector element area of 58%. The improved resolution enabled by the smaller pixel sizes contributed to reducing the volume estimation error from $51.1\% \pm 41.7\%$ to $24.1\% \pm 25.6\%$.

Recent studies by Eberhard et al.,[23] van der Werf et al.,[25] Wolf et al.,[47] and Dobrolinska et al.[48] similarly investigated CAC imaging on the NAEOTOM Alpha PCD-CT with an emphasis on assessing calcium scoring. In those studies, however, the standard detector collimation of 144×0.4 mm was used. Our study used the higher resolution detector collimation of 120×0.2 mm, which was predicted to further decrease calcium blooming artifacts beyond that of the standard resolution. Recent work by Mergen et al.[24] used the UHR detector collimation for coronary CT angiography procedures to evaluate the feasibility and quality in patients with a high CAC load. However, CAC volume quantification was not evaluated. Comparatively, our investigation was primarily focused on assessing further improvements in CAC volume quantification enabled by the UHR collimation.

Our study had several limitations. First, our experimental setup involved *ex vivo* arterial specimens submerged in an anthropomorphic water tank, which lacked the typical anatomical structure located in the human thorax. The attenuation resulting from the 30 cm water tank was, however, a reasonable approximation of a normal weight adult, and the segmentation performed would not have been impacted by lung anatomy. Second, our acquisitions did not include coronary motion. The static assessment of the specimens was considered appropriate for isolating the impact of the UHR collimation. Third, the mass density of the CAC specimens used in this investigation was not known. However, the task of assessing volume quantification, and not calcium score, could be accomplished using micro-CT as a reference standard. Fourth, the HMT was calculated using an ROI that was manually positioned in the calcification by the user. Manual positioning of the ROI may vary slightly from user to user; however, having a single user generate all ROIs across all specimens and scanner systems would produce consistent and comparable results. Finally, the Slice-PKAID CT image denoising algorithm used in this work was developed in house and is not commercially available. The application of Slice-PKAID was found to be successful in this work; however, other CT image-based denoising algorithms could be similarly as effective.

5 Conclusions

This study demonstrated that scanning CACs on a clinical PCD-CT using a UHR collimation yielded reductions in calcium blooming artifacts and improvements in calcification volume quantification accuracy relative to a state-of-the-art EID-CT system. These results are attributed to the improved spatial resolution of the PCD-CT system through use of smaller-sized detector elements and the brighter CNR of PCDs relative to EIDs.

References

1. R. D. Rifkin, A. F. Parisi, and E. Folland, "Coronary calcification in the diagnosis of coronary artery disease," *Am. J. Cardiol.* **44**, 141–147 (1979).
2. W. Liu et al., "Current understanding of coronary artery calcification," *J. Geriatr. Cardiol.* **12**, 668–675 (2015).
3. G. Sangiorgi et al., "Arterial calcification and not lumen stenosis is highly correlated with atherosclerotic plaque burden in humans: a histologic study of 723 coronary artery segments using nondecalcifying methodology," *J. Am. Coll. Cardiol.* **31**, 126–133 (1998).
4. J. A. Rumberger et al., "Coronary artery calcium area by electron-beam computed tomography and coronary atherosclerotic plaque area. A histopathologic correlative study," *Circulation* **92**, 2157–2162 (1995).
5. J. A. Rumberger, "Using noncontrast cardiac CT and coronary artery calcification measurements for cardiovascular risk assessment and management in asymptomatic adults," *Vasc. Health Risk Manag.* **6**, 579–591 (2010).
6. D. C. Goff, Jr. et al., "2013 ACC/AHA guideline on the assessment of cardiovascular risk: a report of the American College of Cardiology/American Heart Association Task Force on Practice Guidelines," *Circulation* 2014;**129**:S49–S73.
7. J. Knuuti et al., "2019 ESC guidelines for the diagnosis and management of chronic coronary syndromes," *Eur. Heart J.* **41**, 407–477 (2020).
8. S. D. Fihn et al., "2012 ACCF/AHA/ACP/AATS/PCNA/SCAI/STS guideline for the diagnosis and management of patients with stable ischemic heart disease: a report of the American College of Cardiology Foundation/American Heart Association task force on practice guidelines, and the American College of Physicians, American Association for Thoracic Surgery, Preventive Cardiovascular Nurses Association, Society for Cardiovascular Angiography and Interventions, and Society of Thoracic Surgeons," *Circulation* **126**, 3097–3137 (2012).
9. A. Lehker and D. Mukherjee, "Coronary calcium risk score and cardiovascular risk," *Curr. Vasc. Pharmacol.* **19**, 280–284 (2021).
10. M. J. Budoff et al., "Diagnostic performance of 64-multidetector row coronary computed tomographic angiography for evaluation of coronary artery stenosis in individuals without known coronary artery disease: results from the prospective multicenter ACCURACY (Assessment by Coronary Computed Tomographic Angiography of Individuals Undergoing Invasive Coronary Angiography) trial," *J. Am. Coll. Cardiol.* **52**, 1724–1732 (2008).
11. J. Abdulla et al., "Influence of coronary calcification on the diagnostic accuracy of 64-slice computed tomography coronary angiography: a systematic review and meta-analysis," *Int. J. Cardiovasc. Imaging* **28**, 943–953 (2012).
12. S. Leng et al., "Photon-counting detector CT: system design and clinical applications of an emerging technology," *Radiographics* **39**, 729–743 (2019).
13. M. J. Willemink et al., "Photon-counting CT: technical principles and clinical prospects," *Radiology* **289**, 293–312 (2018).
14. T. Flohr et al., "Photon-counting CT review," *Phys. Med.* **79**, 126–136 (2020).

15. S. S. Hsieh et al., "Photon counting CT: clinical applications and future developments," *IEEE Trans. Radiat. Plasma Med. Sci.* **5**, 441–452 (2021).
16. S. Leng et al., "Dose-efficient ultrahigh-resolution scan mode using a photon counting detector computed tomography system," *J. Med. Imaging* **3**, 043504 (2016).
17. K. Rajendran et al., "Full field-of-view, high-resolution, photon-counting detector CT: technical assessment and initial patient experience," *Phys. Med. Biol.* **66**, 205019 (2021).
18. W. Zhou et al., "Lung nodule volume quantification and shape differentiation with an ultra-high resolution technique on a photon-counting detector computed tomography system," *J. Med. Imaging* **4**, 043502 (2017).
19. S. Leng et al., "150-μm spatial resolution using photon-counting detector computed tomography technology: technical performance and first patient images," *Invest. Radiol.* **53**, 655–662 (2018).
20. P. VanMeter et al., "Quantification of coronary calcification using high-resolution photon-counting-detector CT and an image domain denoising algorithm," *Proc SPIE* **12031**, 120311R (2022).
21. N. R. van der Werf et al., "Improved coronary calcium detection and quantification with low-dose full field-of-view photon-counting CT: a phantom study," *Eur. Radiol.* **32**, 3447–3457 (2022).
22. R. Symons et al., "Coronary artery calcium scoring with photon-counting CT: first in vivo human experience," *Int. J. Cardiovasc. Imaging* **35**, 733–739 (2019).
23. M. Eberhard et al., "Coronary calcium scoring with first generation dual-source photon-counting CT-first evidence from phantom and in-vivo scans," *Diagnostics* **11**, 1708 (2021).
24. V. Mergen et al., "Ultra-high-resolution coronary CT angiography with photon-counting detector CT: feasibility and image characterization," *Invest. Radiol.* **57**, 780–788 (2022).
25. N. R. van der Werf et al., "Reproducibility of coronary artery calcium quantification on dual-source CT and dual-source photon-counting CT: a dynamic phantom study," *Int. J. Cardiovasc. Imaging* **38**, 1613–1619 (2022).
26. S. A. Si-Mohamed et al., "Coronary CT angiography with photon-counting CT: first-in-human results," *Radiology* **303**, 303–313 (2022).
27. M. Sandstedt et al., "Improved coronary calcification quantification using photon-counting-detector CT: an ex vivo study in cadaveric specimens," *Eur. Radiol.* **31**, 6621–6630 (2021).
28. K. Rajendran et al., "First clinical photon-counting detector CT system: technical evaluation," *Radiology* **303**, 130–138 (2022).
29. S. Tao et al., "Noise reduction in CT image using prior knowledge aware iterative denoising," *Phys. Med. Biol.* **65**, 225032 (2020).
30. Z. S. Hostetler, J. D. Stitzel, and A. A. Weaver, "Comparing rib cortical thickness measurements from computed tomography (CT) and Micro-CT," *Comput. Biol. Med.* **111**, 103330 (2019).
31. T. L. Kline, M. Zamir, and E. L. Ritman, "Accuracy of microvascular measurements obtained from micro-CT images," *Ann. Biomed. Eng.* **38**, 2851–2864 (2010).
32. L. Y. Du et al., "A quality assurance phantom for the performance evaluation of volumetric micro-CT systems," *Phys. Med. Biol.* **52**, 7087–7108 (2007).
33. M. Stauber and R. Müller, "Micro-computed tomography: a method for the non-destructive evaluation of the three-dimensional structure of biological specimens," *Methods Mol. Biol.* **455**, 273–292 (2008).
34. S. M. Jorgensen, O. Demirkaya, and E. L. Ritman, "Three-dimensional imaging of vasculature and parenchyma in intact rodent organs with X-ray micro-CT," *Am. J. Physiol.* **275**, H1103–H1114 (1998).
35. J. Marsh, Jr. et al., "A blooming correction technique for improved vasa vasorum detection using an ultra-high-resolution photon-counting detector CT," *Proc SPIE* **11312**, 113124R (2020).
36. J. F. Marsh, Jr. et al., "Measurement of enhanced vasa vasorum density in a porcine carotid model using photon counting detector CT," *J. Med. Imaging* **10**, 016001 (2023).
37. A. S. Dunning et al., "Accuracy of nodule volume and airway wall thickness measurement using low-dose chest CT on a photon-counting detector CT scanner," *Invest. Radiol.* **58**, 283–292 (2023).
38. T. G. Flohr et al., "Novel ultrahigh resolution data acquisition and image reconstruction for multi-detector row CT," *Med. Phys.* **34**, 1712–1723 (2007).
39. W. Zhou et al., "Comparison of a photon-counting-detector CT with an energy-integrating-detector CT for temporal bone imaging: a cadaveric study," *Am. J. Neuroradiol.* **39**, 1733–1738 (2018).
40. S. Leng et al., "Temporal bone CT: improved image quality and potential for decreased radiation dose using an ultra-high-resolution scan mode with an iterative reconstruction algorithm," *Am. J. Neuroradiol.* **36**, 1599–1603 (2015).
41. K. Taguchi and J. S. Iwanczyk, "Vision 20/20: single photon counting x-ray detectors in medical imaging," *Med. Phys.* **40**, 100901 (2013).
42. A. S. Agatston et al., "Quantification of coronary artery calcium using ultrafast computed tomography," *J. Am. Coll. Cardiol.* **15**, 827–832 (1990).
43. V. Mergen et al., "Tube voltage-independent coronary calcium scoring on a first-generation dual-source photon-counting CT-a proof-of-principle phantom study," *Int. J. Cardiovasc. Imaging* **38**, 905–912 (2021).

44. N. R. van der Werf et al., "Dose reduction in coronary artery calcium scoring using mono-energetic images from reduced tube voltage dual-source photon-counting CT data: a dynamic phantom study," *Diagnostics* **11**, 2192 (2021).
45. N. R. van der Werf et al., "Coronary calcium scores on dual-source photon-counting computed tomography: an adapted Agatston methodology aimed at radiation dose reduction," *Eur. Radiol.* **32**, 5201–5209 (2022).
46. N. Fink et al., "Photon counting detector CT-based virtual noniodine reconstruction algorithm for in vitro and in vivo coronary artery calcium scoring: impact of virtual monoenergetic and quantum iterative reconstructions," *Invest. Radiol.* (2023).
47. E. V. Wolf et al., "Intra-individual comparison of coronary calcium scoring between photon counting detector- and energy integrating detector-CT: effects on risk reclassification," *Front. Cardiovasc. Med.* **9**, 1053398 (2022).
48. M. M. Dobrolinska et al., "Radiation dose optimization for photon-counting CT coronary artery calcium scoring for different patient sizes: a dynamic phantom study," *Eur. Radiol.* **33**, 4668–4675 (2023).

Jeffrey F. Marsh received his BS degree in bioengineering from the University of Illinois at Chicago in 2016. He is now a biomedical engineer working in the Department of Radiology, Mayo Clinic, Rochester, Minnesota, United States. His current research projects involve photon counting detector computed tomography and the application of artificial intelligence in medical imaging.

Patrick D. VanMeter received his PhD in physics from the University of Wisconsin–Madison in 2020 before continuing to a postdoc at the Mayo Clinic CT Clinical Innovation Center. He now works as a data scientist at Certilytics, where he specializes in the application of deep learning to healthcare data. He is a scientist with cross-disciplinary interests and experience in physics, data science, and medical imaging.

Kishore Rajendran received his BE degree in biomedical engineering in 2009 from Anna University, his MS degree in medical electronics in 2011 from Coventry University, and his PhD in radiology in 2016 from the University of Otago. Currently, he is an assistant professor research fellow in the Department of Radiology, Mayo Clinic, Rochester, Minnesota, United States. His current research focuses on photon-counting CT for early detection of vascular diseases, CT image reconstruction, and CT noise reduction.

Shuai Leng received his BS degree in engineering physics in 2001 and his MS degree in engineering physics in 2003 from Tsinghua University, and his PhD in medical physics in 2008 from the University of Wisconsin–Madison. He is an associate professor of medical physics at the Mayo Clinic, Rochester, Minnesota, United States. He has authored more than 160 peer-reviewed articles. His research interest is in technical development and clinical application of x-ray and CT imaging.

Cynthia H. McCollough received her doctorate from the University of Wisconsin in 1991. She is a professor of radiological physics and biomedical engineering at the Mayo Clinic, where she directs the CT Clinical Innovation Center. Her research interests include CT dosimetry, advanced CT technology, and new clinical applications, such as dual-energy and multi-spectral CT. She is an NIH-funded investigator and is active in numerous professional organizations. She is a fellow of the AAPM, ACR, and AIMBE.